

# Geostrophic convective turbulence: The effect of boundary layers

Rodolfo Ostilla-Mónico<sup>1</sup>, Erwin P. van der Poel<sup>1</sup>, Rudie P. J. Kunnen<sup>2</sup>, Roberto Verzicco<sup>3,1</sup> and Detlef Lohse<sup>1</sup>

<sup>1</sup> *Physics of Fluids Group, Mesa+ Institute, and J. M. Burgers Centre for Fluid Dynamics, University of Twente, 7500 AE Enschede, The Netherlands*

<sup>2</sup> *Fluid Dynamics Laboratory, Department of Physics and J.M. Burgers Centre for Fluid Dynamics, Eindhoven University of Technology, P.O. Box 513, 5600 MB Eindhoven, The Netherlands*

<sup>3</sup> *Dipartimento di Ingegneria Industriale, University of Rome “Tor Vergata”, Via del Politecnico 1, Roma 00133, Italy*

(Dated: December 7, 2024)

This Letter presents results of the first direct numerical simulations of rotating Rayleigh–Bénard convection in the so-called geostrophic regime, (hence very small Ekman numbers  $\mathcal{O}(10^{-7})$  and high Rayleigh numbers  $Ra = 10^{10}$  and  $5 \cdot 10^{10}$ ), employing the *full* Navier–Stokes equations. In the geostrophic regime the criteria of very strong rotation and large supercriticality are met simultaneously, which is true for many geophysical and astrophysical flows. Until now, numerical approaches of this regime have been based on *reduced* versions of the Navier–Stokes equations (cf. Sprague *et al.* *J. Fluid Mech.*, **551**, 141 (2006)), omitting the effect of the viscous (Ekman) boundary layers. By using different velocity boundary conditions at the plates, we study the effect of these Ekman layers. We find that the formation of large-scale structures (Rubio *et al.* (*Phys. Rev. Lett.* **112** (2014))), which indicates the presence of an inverse energy cascade, does *not* take place when the Ekman layers are present (i.e., for no-slip plates). For very strong background rotation Ekman pumping is an important source of fluctuations. This causes the heat transfer to be larger for no-slip boundary conditions as compared to stress-free boundary conditions.

Natural convection is ubiquitous in Nature, found not only in the Earth’s interior and oceans, but also in planetary atmospheres and inside stars [1, 2]. In all those instances the background rotation induces a Coriolis force. Rotating Rayleigh–Bénard (RB) flow [3], the flow between two rotating parallel planes, one heated from below and the other cooled from above is commonly used as a model for studying rotating thermal convection.

The addition of an increasingly strong Coriolis force to a rotating RB flow completely changes the flow topology from plume-like structures to columnar vortices [3]. Eventually, if rotation is large enough, and viscosity small enough, owing to the Taylor–Proudman theorem [4], the flow becomes quasi-two-dimensional (Q2D). This implies that all slow large-scale motions become 2D — meaning independent of the direction parallel to the axis of rotation — but there still exist faster and small-scale three-dimensional (3D) dynamics. The large-scale motions exhibit the geostrophic balance between pressure gradient and Coriolis force [4]. This regime of natural convection has been labeled ‘geostrophic turbulence’ by Julien and coworkers [5, 6].

Due to the difficulty of achieving both a high rotation rate and a significant level of turbulence, most experimental and numerical studies of rotating RB have not conclusively reached the geostrophic regime of RB [7–15]. Until the very recent work by Ecke & Niemela [16] the geostrophic regime of RB flow remained elusive in experiments. On the other hand, approaches based on simulating a reduced set of the Navier–Stokes equations [5, 6] have succeeded in expanding the parameter range of rotating convection, proposing scaling relationships for the heat transport in the geostrophic regime [17] and analysing the flow structures [18]. Recently, using these

reduced equations, Rubio *et al.* [19] have shown an inverse energy cascade in the geostrophic regime. In an inverse cascade, unlike the regular cascade of 3D homogeneous isotropic turbulence, energy flows from the small length scales to larger ones. This leads to the formation of large-scale structures that typically become comparable in size to the domain in which they reside. These results have been qualitatively confirmed very recently with DNS of the full equations [20].

Simulations of the reduced Navier–Stokes equation for rapidly rotating Rayleigh–Bénard (RRRB) [5] have been an effective tool thus far. However, the equations are asymptotically reduced, meaning that not the entire physics is included. Furthermore, the equations automatically imply stress-free boundaries which automatically excludes the no-slip-style boundaries with their associated Ekman boundary layers [4].

In this letter we present the first simulations of geostrophic convective turbulence using the full Navier–Stokes equations. We analyse the effects of the choice of boundary conditions, i.e. including or omitting the Ekman layers. We find that the effect of the Ekman layers is crucial and twofold. First, we will show that in the geostrophic regime of RB, the formation of large scale structures, by the inverse energy cascade [19], is limited to the case of two stress-free plates. They are not present if both or even one of the plates is no-slip. A no-slip boundary condition in fact allows for the injection of small-scale vorticity into the flow, precluding the formation of domain-scale vortices and thus hindering the development of an inverse cascade. The second effect is more subtle. In the geostrophic regime the total heat flux can be *lower* for stress-free plates than for no-slip plates. This is again due to increased turbulence induced in the

flow by the Ekman layers due to the so-called Ekman pumping, as well as the inhibition of the formation of large-scale vortices which have been shown to reduce the overall heat flux [21]. Thus, the applied boundary conditions can have a far-reaching non-intuitive effects in the geostrophic regime.

We have conducted a set of DNSs of 3D rotating RB in a horizontally periodic cartesian box, employing the full Navier–Stokes equations. We proceed as follows: starting from a simulation with no-slip bottom and top plates, i.e. for which  $\mathbf{u} = \mathbf{0}$  at the plates, where  $\mathbf{u}$  is the fluid velocity, we switch the velocity boundary conditions (BCs) at the plates to be stress-free, i.e.  $\partial_n \mathbf{u}_t = 0$  and  $\mathbf{u}_n = 0$  with  $n$  the direction normal to the plate, and  $t$  that parallel, at either one (the top) or both plates and observe the dynamical properties of each of these systems diverge from each other. Simulations were done using a second-order finite difference code with fractional time-stepping [22]. As common, centrifugal buoyancy can be neglected in this regime, and thus the following equations are solved:

$$\nabla \cdot \mathbf{u} = 0, \quad (1)$$

$$\frac{\partial \mathbf{u}}{\partial t} + \mathbf{u} \cdot \nabla \mathbf{u} + Ro^{-1} \mathbf{e}_z \times \mathbf{u} = -\nabla p + \sqrt{\frac{Ra}{Pr}} \nabla^2 \mathbf{u} + \theta \mathbf{e}_z, \quad (2)$$

$$\frac{\partial \theta}{\partial t} + \mathbf{u} \cdot \nabla \theta = \sqrt{\frac{1}{RaPr}} \nabla^2 \theta, \quad (3)$$

where  $t$  is time,  $\mathbf{e}_z$  is the unit vector in the vertical direction,  $Ra$  is the Rayleigh number, i.e. the non-dimensional temperature difference, defined as  $Ra = g\beta\Delta L^3/(\nu\kappa)$  with  $L$  the height of the sample,  $\beta$  is the thermal expansion coefficient of the fluid,  $g$  the gravitational acceleration,  $\Delta$  the temperature difference between bottom and top of the sample, and  $\nu$  and  $\kappa$  the kinematic viscosity and thermal diffusivity of the fluid, respectively.  $Ro$  is the Rossby number, i.e. the inverse rotation, defined as  $Ro = \sqrt{\beta g \Delta / L} / (2\Omega)$ , where  $\Omega$  is the angular rotation rate,  $Pr = \nu/\kappa$  is the Prandtl number of the fluid (here fixed to one), and  $\theta$  the non-dimensional temperature. Equations (1)–(3) are shed in their current dimensionless forms by scaling with  $L$ ,  $\Delta$ , and the free-fall velocity scale  $\sqrt{\beta g \Delta L}$ .

The Rayleigh number was varied between  $Ra = 10^{10}$  and  $Ra = 5 \cdot 10^{10}$ , while the Rossby number was varied between  $Ro = 0.04$  and  $Ro = 0.09$ , i.e. in the strongly rotating regime. This resulted in Ekman numbers  $Ek = Ro\sqrt{Pr/Ra}$  in the range  $Ek = 1.9 \cdot 10^{-7}$  to  $Ek = 9 \cdot 10^{-7}$ , which is within the geostrophic regime as  $Ek < 10^{-6}$  [17]. The aspect-ratio  $\Gamma = D/L$ , where  $D$  is the simulation box periodicity in the horizontal directions, was set to ten times the most unstable wavelength for convective instability, i.e.  $\Gamma = 10L_c = 48.2Ek^{1/3}$  [23]. Temperature BCs were taken as fixed temperature,  $\theta = 1$

at the bottom plate and  $\theta = 0$  at the top plate. The full details on the conducted runs and the applied resolutions are presented in Table I.

All simulations are started from the same initial conditions, namely a statistically stationary no-slip RRRB case with the same parameters. From this initial condition, the velocity BCs are either kept or switched at the first time step: we consider also the cases of a stress-free top plate and both plates stress-free. They were then advanced in time for at least 100 non-dimensional time units, and even more in the case of stress-free/stress-free BCs. In that latter case, after some time, large-scale structures start to appear similar to Refs. [19–21]. These remain absent in both the no-slip/no-slip and no-slip/free-slip configurations.

Figure 1 shows an instantaneous contour plot of the vertical vorticity,  $\omega_z = \partial_x u_y - \partial_y u_x$  in the mid-gap for  $\tilde{t} = 100$  for the no-slip/no-slip and stress-free/stress-free plate cases with  $Ra = 10^{10}$  and  $Ro = 0.09$ . The large cyclonic vortex (vorticity of like sign as the background rotation, i.e. positive in this case) is clearly identified in the left panel, where the bottom-left part hints at a rather weak anticyclone. Such large-scale structures are definitely not seen in the right panel. The same is true for the asymmetric plate configuration, not shown in the figure.

It is worth noting that the total  $\omega_z$  in a horizontal plane must be zero. An exact cyclone/anticyclone symmetry is only recovered for the case of infinite background rotation rate, where an additional symmetry is gained. This is the case of the reduced equations [5], and thus a perfect symmetry can be seen in Rubio *et al.* [19]. In our simulations, we do not recover this symmetry exactly as  $Ro$  remains finite, and there is a clear preference for a large cyclone surrounded by tiny patches of anticyclonic vorticity. This effect is also reflected in the skewness of the vertical vorticity, which is always positive.

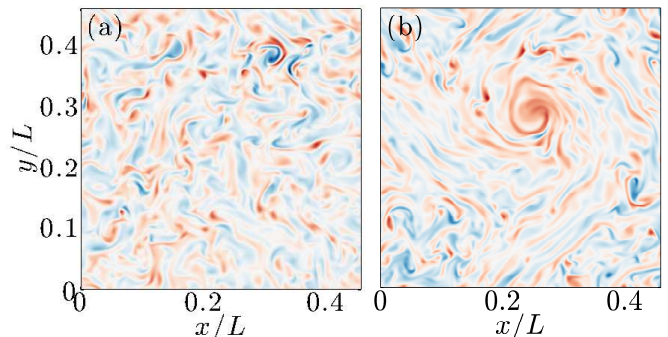


FIG. 1. Contour plots of the vertical vorticity  $\omega_z$  at  $\tilde{t} = 100$  in the mid-plane for BCs with no-slip/no-slip BCs (top) and stress-free/stress-free BCs (bottom) for  $Ra = 10^{10}$  and  $Ro = 0.09$ . Red is positive (cyclonic) vorticity, while blue is negative (anticyclonic) vorticity. Both contour plots have the same color scale.

The temporal evolution of the large-scale structure can be quantified as follows: we first define the horizontal kinetic energy  $k_H$ , as  $k_H = \frac{1}{2}(u_x^2 + u_y^2)$ . We then apply a Fourier transform in both horizontal directions to both  $k_H$  and  $\omega_z$ . We can then use the two Fourier components associated to the fundamental frequencies (i.e. those with the largest wavelength) to get an idea of the strength of motions on the largest scales allowed in this domain.

Figure 2 shows the time evolution of the fundamental Fourier components of both  $k_H$  and  $\omega_z$ . As expected from Figure 1, a very large growth can be seen for the stress-free/stress-free case, while only a very moderate growth can be seen for the no-slip/stress-free case. There is no growth whatever for the no-slip/no-slip case. In the stress-free/stress-free case, after almost 140 non-dimensional time units, there seems to a saturation of the energy content of the cyclone/anti-cyclone pair, even if the total heat transport and other average quantities remain relatively unchanged during the growth. The wavelength of the cyclone cannot grow past the box size, and it is very likely that if the horizontal periodic length of the system was larger, the structure would grow to occupy the whole domain. The mechanism by which these cyclones and anticyclones form was already studied in detail by Refs. [19, 20], and we will not repeat it here.

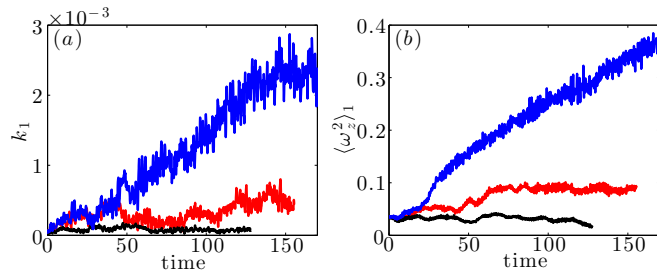


FIG. 2. Time evolution of the fundamental Fourier components of  $k_H$  and  $\omega_z$  for stress-free/stress-free (blue), no-slip/stress-free (red) and no-slip/no-slip (black) BCs for  $Ra = 10^{10}$  and  $Ro = 0.09$ . The values grow, but eventually saturate for no-slip/stress-free BCs. For the stress-free/stress-free BCs, the energy is not seen to saturate until  $t \approx 140$ .

A summary of the effect of the different BCs and thus of the large-scale structure on the heat transport is shown in Table I. Heat transport is non-dimensionalized as a Nusselt number  $Nu = (\langle u_z T \rangle_{A,t} - \langle \partial_z T \rangle_{A,t}) / (\kappa \Delta L^{-1})$ , where  $\langle \dots \rangle_{A,t}$  denotes averaging with respect to time and in a plane  $A$  parallel to the end plates. For the time averaging, the initial transients have been cut out. For the stress-free/stress-free case, even if the large scale structures have not yet saturated, the Nusselt number appears to reach a statistically stationary state after a smaller time.

We note that for large enough rotation (small enough  $Ro$ ), the case with no-slip/no-slip plates has a *higher*  $Nu$  than the corresponding case with stress-free/stress-free

plates. This is unlike any other simulations of RB, including rotating RB, previously reported in the literature. We can attribute this heat transport effect to small-scale fast motions. Reduction of vertical fluctuations by rotation leads to reduced mixing in the flow, and thus a reduced heat transport. This mechanism was previously proposed by Sprague *et al.* [5], as an explanation for reduced heat transport in the geostrophic regime. However, the no-slip cases have an additional source of vertical fluctuations, namely Ekman pumping. Additionally, it has been shown for stress-free plates that the large-scale vortex itself acts as a barrier to heat transfer [21].

Comparing our Nusselt number results for the stress-free/stress-free cases to Refs. [5, 6], it is found that the run at  $Ro = 0.04$  reveals a good quantitative agreement while for higher  $Ro$  an increasing discrepancy is found, with the current  $Nu$  values from the full Navier-Stokes simulations being larger. Thus these parameters form an indication of the range of applicability of the reduced equations [5].

To illustrate and quantify the changes to the vertical-velocity fluctuations, figure 3 shows the vertical dependence of the rms vertical velocity  $u'_z$ . This is an indicator not only of the fluctuations in the system which are the ones responsible for heat transport, but also a measure of the degree of geostrophy of the flow. At the lowest  $Ro = 0.04$ , the fluctuations due to the Ekman layers of the no-slip/no-slip case cause an overall higher level of fluctuations in the domain compared to the stress-free/stress-free case (red and blue lines, respectively), which increases heat transport. At higher  $Ro = 0.09$ , this effect loses importance and the fluctuations of the free-slip/free-slip case become larger than for no-slip/no-slip (magenta and black lines, respectively). This explains the relatively larger  $Nu$  in no-slip/no-slip BCs. The different signatures of Ekman layers are clearly visible from figure 3: they reveal a considerably steeper rise of vertical velocity fluctuations near  $z/L = 0$  (compare magenta and red lines to black and blue lines). The “kink” in the red line, (see arrow), indicates the edge of the Ekman BL, which is thinner than the thermal BL at these parameters.

In conclusion, this letter presents the first DNS of the full Navier–Stokes equations in the geostrophic regime. The effect of the velocity boundary conditions on the flow was found to be crucial for overall flow structure and heat transfer. The presence of a no-slip BC, and thus of an Ekman layer, induces significant fast small-scale motions due to Ekman pumping. These motions inhibit the formation of large-scale structures, which are seen when both BCs are stress-free [19, 21] and saturate in size only due to the finite simulation domain. These simulations are also the first example of a *lower* heat transport occurring for stress-free BCs when compared to no-slip BCs. In the parameter space explored until now this has not yet occurred been the case [9, 13]. This striking effect

B/T BCs	Ra	Ro	Ek	$\widetilde{\text{Ra}}$	$\Gamma$	$N_x \times N_y \times N_z$	$Nu$
NS/NS	$1 \cdot 10^{10}$	0.09	$9.00 \cdot 10^{-7}$	86.9	0.46	$384 \times 384 \times 768$	$50.2 \pm 0.5$
NS/SF	$1 \cdot 10^{10}$	0.09	$9.00 \cdot 10^{-7}$	86.9	0.46	$384 \times 384 \times 768$	$47.9 \pm 1.1$
SF/SF	$1 \cdot 10^{10}$	0.09	$9.00 \cdot 10^{-7}$	86.9	0.46	$384 \times 384 \times 768$	$46.2 \pm 0.1$
NS/NS	$5 \cdot 10^{10}$	0.04	$1.79 \cdot 10^{-7}$	50.4	0.27	$512 \times 512 \times 1024$	$30.8 \pm 0.5$
SF/SF	$5 \cdot 10^{10}$	0.04	$1.79 \cdot 10^{-7}$	50.4	0.27	$512 \times 512 \times 1024$	$18.3 \pm 0.1$
NS/NS	$5 \cdot 10^{10}$	0.066	$2.95 \cdot 10^{-7}$	98.2	0.32	$512 \times 512 \times 1024$	$61.6 \pm 0.3$
SF/SF	$5 \cdot 10^{10}$	0.066	$2.95 \cdot 10^{-7}$	98.2	0.32	$512 \times 512 \times 1024$	$55.1 \pm 0.3$
NS/NS	$5 \cdot 10^{10}$	0.09	$4.02 \cdot 10^{-7}$	148.3	0.36	$512 \times 512 \times 1024$	$88.2 \pm 0.7$
SF/SF	$5 \cdot 10^{10}$	0.09	$4.02 \cdot 10^{-7}$	148.9	0.36	$512 \times 512 \times 1024$	$101 \pm 2.2$

TABLE I. Details of the conducted numerical simulations. The first column shows the boundary conditions at the bottom and top plates (‘B/T’), where ‘NS’ stands for no-slip and ‘SF’ for stress-free. The three next columns show the applied control parameters. The Prandtl number is always  $\text{Pr} = 1$ . The fifth column shows  $\widetilde{\text{Ra}} = \text{RaEk}^{4/3}$  [5]. The corresponding supercriticality  $\text{Ra}/\text{Ra}_c$  [16] ( $\text{Ra}_c$  is the critical Ra for the onset of convection [23]) is easily found as  $\widetilde{\text{Ra}}/8.7$ ; the minimal supercriticality used here is 5.8 at  $\widetilde{\text{Ra}} = 50.4$ . The sixth column shows the aspect ratio, the horizontal periodicity length divided by  $L$ , while the seventh column shows the numerical resolutions. The final column shows the Nusselt number, the non-dimensionalized heat transport between the plates, with the error estimation due to temporal fluctuations.

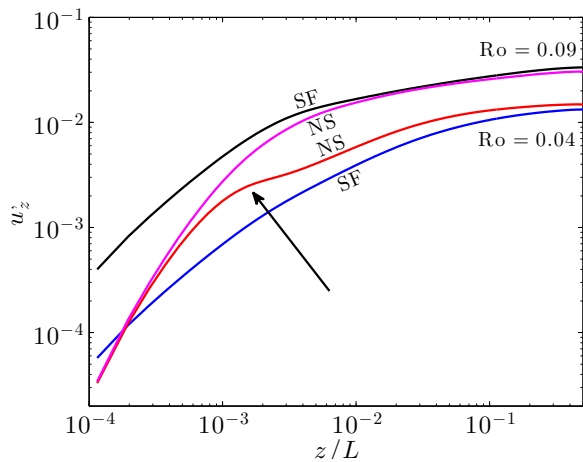


FIG. 3. Rms of vertical velocity  $u'_z$  for  $\text{Ra} = 5 \cdot 10^{10}$  and  $\text{Ro} = 0.04$  and no-slip/no-slip plates (red), stress-free/stress-free plates (blue) and for  $\text{Ro} = 0.09$  and no-slip/no-slip plates (magenta), stress-free/stress-free plates (black). For lower  $\text{Ro}$ , the fluctuations of the no-slip/no-slip case are higher throughout the Ekman layer and bulk. These originate in the Ekman layer. The end of this layer causes a “kink” in the fluctuations (marked with an arrow on the panel). For higher  $\text{Ro}$ , the fluctuations are larger for the stress-free/stress-free case.

shows up for strong enough rotation is strong: The no-slip cases have Ekman pumping as an additional source of fluctuations and heat transport becomes larger than for the stress-free cases. We hope to be able to proceed further into this new, highly relevant regime of rotating convection.

*Acknowledgments:* We would like to thank S. Grossmann, C. Sun, and Y. Yang for various stimulating discussions. We acknowledge FOM, an ERC Advanced Grant and the PRACE resource Hermit, based in Stuttgart at HLRS.

- [1] J. A. Glazier, T. Segawa, A. Naert, and M. Sano, *Nature* **398**, 307 (1999).
- [2] M. Heimpel, J. Aurnou, and J. Wicht, *Nature* **438**, 193 (2005).
- [3] R. J. A. M. Stevens, H. J. H. Clercx, and D. Lohse, *Eur. J. Mech. B/Fluids* **40**, 41 (2013).
- [4] J. Pedlosky, *Geophysical Fluid Dynamics* (Springer-Verlag, Berlin, Heidelberg, 1987).
- [5] M. Sprague, K. Julien, E. Knobloch, and J. Werne, *J. Fluid Mech.* **551**, 141 (2006).
- [6] K. Julien, M. A. Rubio, I. Grooms, and E. Knobloch, *Geophys. Astrophys. Fluid Dyn.* **106**, 392 (2012).
- [7] H. T. Rossby, *J. Fluid Mech.* **36**, 309 (1969).
- [8] F. Zhong, R. E. Ecke, and V. Steinberg, *J. Fluid Mech.* **249**, 135 (1993).
- [9] K. Julien, S. Legg, J. McWilliams, and J. Werne, *J. Fluid Mech.* **322**, 243 (1996).
- [10] Y. Liu and R. E. Ecke, *Phys. Rev. Lett.* **79**, 2257 (1997).
- [11] J. Q. Zhong, R. J. A. M. Stevens, H. J. H. Clercx, R. Verzicco, D. Lohse, and G. Ahlers, *Phys. Rev. Lett.* **102**, 044502 (2009).
- [12] E. King, S. Stellmach, J. Noir, U. Hansen, and J. M. Aurnou, *Nature* **457**, 301 (2009).
- [13] S. Schmitz and A. Tilgner, *Geophys. & Astroph. Fluid Dyn.* **104**, 481 (2010).
- [14] R. Kunnen, B. Geurts, and H. Clercx, *J. Fluid Mech.* **642**, 445 (2010).
- [15] S. Horn and O. Shishkina, *Phys. Fluids* **26**, 055111 (2014).
- [16] R. E. Ecke and J. J. Niemela, *Phys. Rev. Lett.* **11**, 114301 (2014).
- [17] K. Julien, E. Knobloch, A. M. Rubio, and G. M. Vasil, *Phys. Rev. Lett.* **109**, 254503 (2012).
- [18] D. Nieves, A. M. Rubio, and K. Julien, *Phys. Fluids* **26**, 086602 (2014).
- [19] A. M. Rubio, K. Julien, E. Knobloch, and J. B. Weiss, *Phys. Rev. Lett.* **112**, 144501 (2014).
- [20] M. P. B. Favier, L.J. Silvers, *Phys. Fluids* (2014), sub-

- mitted, arXiv: 1403.7442.
- [21] C. Guervilly, D. W. Hughes, and C. A. Jones, *J. Fluid Mech.* (2014), submitted, arXiv: 1403.7442.
- [22] R. Verzicco and P. Orlandi, *J. Comput. Phys.* **123**, 402 (1996).
- [23] S. Chandrasekhar, *Hydrodynamic and Hydromagnetic Stability* (Dover, New York, 1981).